



# Anisotropic vacancy-mediated phonon mode softening in Sm and Gd doped ceria<sup>†</sup>

Dong-Hyuk Jung,<sup>‡</sup> Ji-Hwan Lee,<sup>‡</sup> Mehmet Emin Kilic<sup>‡</sup> \* and Aloysius Soon<sup>‡</sup> \*

Cite this: *Phys. Chem. Chem. Phys.*, 2018, 20, 10048

Received 25th January 2018,  
Accepted 8th March 2018

DOI: 10.1039/c8cp00559a

rsc.li/pccp

Ceria doped with Sm and Gd (SDC and GDC) has been suggested as a promising candidate for the electrolyte used in solid oxide fuel cells (SOFCs), since it has relatively high oxygen ion conductivity at intermediate temperature. There have been many previous experimental and computational studies to investigate the properties, structure, and effect of vacancies, etc. for SDC and GDC. However, in these previous studies, it is commonly assumed that the interaction between oxygen vacancies is negligible and many focus only on the mono-vacancy system. In addition, the possibility of anisotropic vibrational motion of the oxygen ions around vacancies is often neglected. In this paper, using both first-principle density-functional theory and classical molecular dynamics calculations, we investigate the structural and vibrational properties of the optimized SDC and GDC structures, such as bonding analysis, phonon density-of-state and mean-square-displacement of the oxygen ions. Also, we report the direction-dependent vibrations at the specific frequency of the oxygen ions near the vacancies, activation energies, and diffusion coefficients of SDC and GDC which can extend our understanding of diffusion dynamics in doped ceria-based electrolytes for SOFC applications.

## 1. Introduction

Solid oxide fuel cells (SOFCs) have been widely investigated as an essential component for a sustainable energy system.<sup>1–4</sup> To increase the practicality and competitiveness by reducing the operation temperature,<sup>5</sup> many studies have tried to find suitable electrolyte materials showing enhanced conductivity in the intermediate temperature (IT) range (773 to 1073 K).<sup>1,2,6,7</sup> With a fairly accessible cavity within its octahedral holes, fluorite-structured oxides such as ceria (CeO<sub>2</sub>) are very promising candidates for SOFCs, but are currently not used mainly due to high reduction temperatures and other problems during sintering. To overcome these hurdles, doping ceria with the rare-earth (RE) elements (such as Sm and Gd) has received particular attention and permits high ion-conduction with lowering of reduction temperatures.

Aliovalent doping with RE elements in these fluorite-structured oxides inevitably results in a charge compensation mechanism (*i.e.* due to the lower oxidation number of RE(3+) than Ce(4+) in CeO<sub>2</sub>), leading to high concentrations of oxygen vacancies, and thus accounting for the commonly observed vacancy-mediated mobile oxygen ion diffusion process in these oxides.<sup>3–6,8,9</sup> The fluorite structure of doped ceria also appears to vary almost linearly with the concentration of dopants, obeying the well-known Vegard's law.<sup>8–12</sup> Amongst various concentrations, it was reported that 10 to 15 mol% of Sm or Gd doped ceria (abbreviated as SDC and GDC, respectively) is considered as the most appropriate electrolyte in IT-SOFCs, as studied both in theory<sup>8,12</sup> and experiments.<sup>9–11</sup>

To get a more detailed atomistic picture of vibrational/thermal and migration properties of SDC and GDC, there have been a few reported theoretical studies examining their atomic and lattice structures. Using a mono-vacancy in the unit cell system, it was reported that the vacancy prefers to form near the RE dopant.<sup>5,12</sup> Other studies attempted to model a more realistic system by including two oxygen vacancies and four Sm atoms in a CeO<sub>2</sub>(2 × 2 × 2) supercell.<sup>13</sup> Through an extensive screening of 3.5 billion Sm<sub>0.125</sub>Ce<sub>0.875</sub>O<sub>1.94</sub> structures using a density-functional theory (DFT)-based sampling framework, they concluded that the oxygen vacancies prefer to be located at about 6 Å in distance from one another.<sup>13</sup>

Such atomic and lattice structural information can have a potential influence on the further investigations of ionic conductivity ( $\sigma$ ) of doped-ceria, often expressed as an Arrhenius-type

Department of Materials Science and Engineering, Yonsei University, Seoul 03722, Korea. E-mail: mekilic@yonsei.ac.kr, aloysius.soon@yonsei.ac.kr

<sup>†</sup> Electronic supplementary information (ESI) available: The calculated structural, electronic and vibrational properties of bare and defected ceria systems: the ground state with energies as a function of volume, lattice constants, bulk modulus, formation energy, XRD, ELF plot, the average values for center of vibration density-of-state, phonon density-of-state plots without weighted and electronic density-of-state for the oxygen around the vacancy; interatomic potential parameters of SDC and GDC, and diffusion coefficient values for homogeneous and randomized SDC and GDC systems. See DOI: 10.1039/c8cp00559a

<sup>‡</sup> Contributed equally to this work.

exponential function with two key parameters: the activation energy barrier ( $E_a$ ) and its pre-factor ( $\sigma_0$ ). In terms of  $E_a$ , it is commonly determined using transition state theory for a single oxygen ion near the oxygen vacancy, in which the vibrational motions of all other oxygen ions are assumed to be completely equilibrated each time a new diffusive event takes place.<sup>5,7,14</sup> This assumption is commonly used for complementary kinetic Monte-Carlo based analysis as well.<sup>15</sup>

Of late, these vibrational properties of defected ceria have been calculated in detail and are shown to be correlated to its ionic conductivity,<sup>16,17</sup> with rather similar vibrational characteristics near these oxygen vacancies.<sup>18,19</sup> However, it is still not clear if this holds true for doped ceria where the oxygen ions near the oxygen vacancies and dopants may exhibit anisotropic vibrational properties. This will then have direct implications on its (enhanced) ionic conductivity.

To verify that, the present work focuses on a systematic investigation of the atomic and lattice structures, vibrational, and migration properties of defected ceria where more than one oxygen vacancy is considered. In particular, to examine the vibrational properties of oxygen ions near the oxygen vacancy and the dopant, we have performed DFT lattice dynamics calculations for ordered structures of ceria, SDC, and GDC. Moreover, to examine the migration properties of oxygen ions in doped ceria for various finite temperatures, diffusion dynamics for both ordered and randomized GDC and SDC are also studied *via* classical molecular dynamics simulations.

## II. Methodology

### A. Density-functional theory calculations

The first-principles calculations based on density-functional theory (DFT) are performed using the Vienna *Ab initio* Simulation Package (VASP) code.<sup>20,21</sup> The projector augmented-wave (PAW)<sup>22,23</sup> method is employed. Specifically, the PAW potentials for the Sm and Gd dopant atoms are chosen to reproduce the 3+ valence state with treating the f electrons as localized core states.<sup>15</sup> The considered exchange–correlation (xc) functional is described using the generalized gradient approximation (GGA) due to Perdew, Burke, and Ernzerhof (PBE).<sup>24</sup> In addition, the optimum on-site Coulomb interaction,  $U_{\text{eff}}$ ,

is needed to agree with experimental 4f band positions. Therefore, an effective Hubbard term ( $U_{\text{eff}} = 4.5$  eV) is only considered for the Ce 4f states.<sup>25,26</sup>

A plane-wave kinetic cutoff energy of 500 eV is used for all DFT calculations to expand the wave functions in a plane-wave basis set. For the Brillouin-zone integrations are performed using a  $\Gamma$ -centered  $k$ -point grid of  $(12 \times 12 \times 12)$  for the primitive  $\text{CeO}_2$  unit cell and is folded with keeping similar  $k$ -points sampling for the  $(2 \times 2 \times 2)$  supercell calculations. The convergence criteria for the total energies and forces are set within  $10^{-5}$  eV and  $0.02$  eV  $\text{\AA}^{-1}$ , respectively. The considered cutoff energy and  $k$ -grid densities are tested within these criteria.

A  $(2 \times 2 \times 2)$  supercell of conventional cubic  $\text{CeO}_2$  (containing 96 atoms, which has been tested for the convergence of phonon vibration modes) is used to examine the vibrational properties in Sm (and Gd) doped ceria. This achieves a stoichiometry of  $\text{Ce}_{0.875}\text{M}_{0.125}\text{O}_{1.9375}$  where M is taken as either Gd or Sm. The positions of the oxygen vacancies and dopant atoms are considered using the most energetically favorable sites as previously determined by a genetic algorithm (see ref. 13 for more details). The vacancy position is defined as the center of the tetrahedrons formed by the nearby cations (Ce, Sm, or Gd) as shown in Fig. 1. Here, we have optimized and determined the lattice constants for each doped and undoped ceria-based system using the 3rd order Birch–Murnaghan equation of state<sup>27,28</sup> (more details can be found in the ESI†).

The radial distribution functions (RDF) for these ceria-based systems are derived to characterize their atomic geometries *via* ring statistics as implemented in the RINGS code.<sup>29,30</sup> Details for the RDF ( $g_{\alpha\beta}(r)$ ) and XRD analysis are elaborated in the ESI.†<sup>31,32</sup>

Using the density-functional perturbation theory (DFPT) method as implemented in the VASP code, phonon frequencies at a constant volume are calculated using the supercell model (as described above) with the Phonopy code.<sup>33,34</sup> The longitudinal optical (LO) and transverse optical (TO) (LO–TO) splitting is also explicitly included considering the Born effective charge tensors and dielectric constants for each ceria-based system.<sup>35</sup>

To better mimic the inelastic neutron scattering experiments, the neutron scattering weighted/corrected phonon vibration density-of-states as function of frequency ( $\nu$ ),  $f_w(\nu)$  is obtained using:

$$f_w(\nu) = \frac{\sigma_{\text{scat}}}{m} f_{\text{DFT}}(\nu), \quad (1)$$

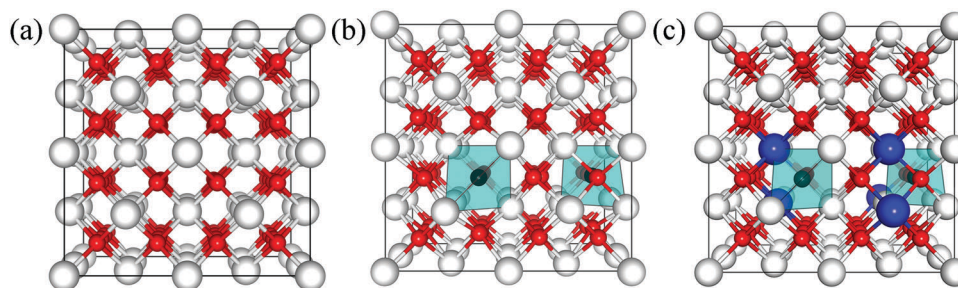


Fig. 1 Optimized atomic geometries of (a) pristine  $\text{CeO}_2$ , (b) oxygen vacancies in  $\text{CeO}_2$  ( $\text{CeO}_{2-x}$ , VAC), and (c) Sm or Gd dopants in  $\text{CeO}_{2-x}$ . Note that a  $(2 \times 2 \times 2)$  supercell model is shown. Here, the oxygen vacancies,  $V_{\text{O}}$  are taken as the geometric center of tetrahedrons consisting of nearest cations (Ce, Sm, or Gd). The white, red, blue and black spheres represent the Ce, O, dopant (Sm or Gd) and  $V_{\text{O}}$ , respectively.

where  $f_{\text{DFT}}(\nu)$  is the DFT-derived phonon vibration density-of-states (vDOS),  $\sigma_{\text{scat}}$  is the total cross section for neutron scattering, and  $m$  is the atomic mass of each element. Here, the  $\sigma_{\text{scat}}$  values for each element are given by 2.94, 180.2, 39.4, and 4.233 for Ce, Gd, Sm, and O, respectively.<sup>36–38</sup>

To aid our discussion and comparison of the calculated vDOS for different ceria-based systems, the representative center of the vDOS band ( $\nu_{\text{center}}$ ) is taken as a first momentum of vDOS:

$$\nu_{\text{center}} = \frac{\int \nu f(\nu_i) d\nu_i}{\int f(\nu_i) d\nu_i}, \quad (2)$$

where the integration here is performed using the trapezoid rule. We note that the influence of the LO–TO splitting on the calculated/corrected vDOS is found to be negligible, in agreement with other theoretical work.<sup>18</sup>

The electron localization function (ELF)<sup>39</sup> (see ESI†) is calculated using the Kohn–Sham DFT orbitals,  $\phi_i$ , to examine the chemical bonding environment for the oxygen ions near the oxygen vacancies and dopants.

### B. Molecular dynamics simulations

The classical molecular dynamics (MD) simulations are performed using the LAMMPS code.<sup>40,41</sup> The potential of interatomic interaction between  $i$  and  $j$  ions is considered as a Buckingham-type with a long-range Coulombic term:

$$V(r_{ij}) = \frac{q_i q_j}{r_{ij}} + A_{ij} \exp\left(-\frac{r_{ij}}{\rho_{ij}}\right) - \frac{C_{ij}}{r_{ij}^6}, \quad (3)$$

where  $q_i$  holds for the charge of ion  $i$  (and likewise,  $q_j$  for ion  $j$ ),  $r_{ij}$  is the interionic distance, and other parameters  $A_{ij}$ ,  $\rho_{ij}$  and  $C_{ij}$  are used to represent the short range terms for each element, Ce–O, Gd–O, Sm–O, and O–O as listed in Table S2 in the ESI.† The reliability of this potential parameter (as compared with experimental data) has been discussed in detail in ref. 42 and 43. In the case of cation–cation interactions, forces are assumed to be purely Coulombic. It is considered that the systems studied in this work are fully ionic where the ionic charges are chosen to be 4+, 3+, 3+, and 2– for Ce, Gd, Sm, and O, respectively. The Buckingham-type potential model has already been successfully employed to describe the dynamics behavior of ceria-based materials in previous literature reports.<sup>44–46</sup>

For the MD calculations, a statistical approach is assumed to present agreement with experimental results since the distributions of ions and defects in crystalline electrolytes are strongly inhomogeneous. With this in mind, the positions of dopant ions in ceria structures are also considered as inhomogeneous by using random number generation. The illustration of doped ion distributions for ordered (homogeneous) doped ceria and randomly (inhomogeneous) doped ceria are compared in Fig. S2 in the ESI.† Here, we adopt two ( $6 \times 6 \times 6$ ) supercell models based on cation dopant distributions for  $\text{Ce}_{0.875}\text{M}_{0.125}\text{O}_{1.9375}$ : ordered doped ceria structures from DFT calculations (in Fig. 1) and a series of randomly distributed doped ceria structures (in Fig. S2 in ESI.†). All supercell models are constructed from a

pristine cubic  $\text{CeO}_2$  lattice. The length of the MD simulation supercell (containing 2538 atoms) for all systems is taken as 32.96 Å and with periodic boundary conditions applied. To achieve electronic neutrality of the system, every two 3+ dopant ions in the systems will be compensated by one oxygen vacancy. The time step used for the integration of Newton's equations of motion is set to 0.5 femtoseconds (fs). All ionic diffusion analyses are then performed using the thermally-quenched structures, considering the temperature ranging from 600 to 1800 K. The detailed steps of the MD calculations to optimize the structure and to calculate the diffusion coefficient ( $D$ ) and activation energy ( $E_a$ ) are given in the ESI.†<sup>47</sup>

## III. Results and discussion

### A. Atomic and electronic structure

The calculated bulk properties of  $\text{CeO}_2$  are close to previously reported theoretical and experimental values: The lattice constant is found to be 5.49 Å, agreeing well with the established theoretical values of 5.36 (LDA)<sup>26</sup> and 5.49 Å (PBE+ $U$ ),<sup>8,48</sup> respectively. Here, the semi-local  $xc$  functional (PBE+ $U$ ) is known to slightly overestimate the bond length with respect to experiments (5.41 Å).<sup>8,49</sup>

To construct and model the appropriate SDC and GDC systems in SOFC applications, we focus on the following for building the atomic models: the stoichiometry of SDC or GDC, the position of dopant atoms, and that of the oxygen vacancies. With this in mind, we have collected extensive atomic and lattice structure information from previous studies.<sup>9–11,13,50–56</sup>

Based on the activation energy of diffusion ( $E_a$ ), it has been reported that  $\text{Ce}_{0.90}\text{M}_{0.10}\text{O}_{1.95}$ <sup>10,52</sup> has the lowest  $E_a$  (of 0.6 eV). Following this, we have constructed our doped ceria atomic structure models based on  $\text{Ce}_{0.875}\text{M}_{0.125}\text{O}_{1.9375}$ , where the M represents Gd or Sm. Next, the energetically-favored positions for the aliovalent dopants and oxygen vacancies ( $\text{V}_\text{O}^\bullet$ ) are then determined, taking references from previous studies.<sup>12,13,57</sup> It has been established that the  $\text{V}_\text{O}^\bullet$  prefers the nearest neighbor site of the aliovalent dopant (Gd<sup>12</sup> or Sm<sup>13</sup>). In addition, *via* a DFT+ $U$  genetic algorithm search of various doped ceria systems, Ismail *et al.* has confirmed that dopants prefer to be paired in ceria.<sup>13</sup>

In order to determine the ground state for each ceria-based system, the total DFT energies as function of volume are fitted to a 3rd order Birch–Murnaghan equation of state<sup>28</sup> (see Fig. S1 and Table S1 in ESI.†). We find that the lattice constants for  $\text{CeO}_{2-x}$ , SDC, and GDC are generally larger than the pristine, defect-free  $\text{CeO}_2$ , and with a corresponding smaller bulk modulus, as reported in previous work.<sup>8</sup> Comparing the other PBE+ $U$  results of the highly doped  $\text{Ce}_{0.75}\text{Sm}_{0.25}\text{O}_2$  and  $\text{Ce}_{0.75}\text{Gd}_{0.25}\text{O}_2$  (5.49 Å and 5.47 Å, respectively) in ref. 8, our PBE+ $U$  results seem to agree better if the linear Vegard's law is assumed.

Moreover, the  $\text{CeO}_{2-x}$  model correctly reflects a lattice cell expansion when compared to pristine  $\text{CeO}_2$  or doped systems (SDC and GDC). This effect is commonly discussed in the literature as the chemical expansion of cations missing

chemical bonds with nearest oxygens (typically when oxygen vacancies are formed). Upon forming the oxygen vacancies (without dopants), the change from  $\text{Ce}^{4+}$  to  $\text{Ce}^{3+}$  near the oxygen vacancy is formally noted. In SDC and GDC, the influence of this chemical expansion of Ce cations is greatly reduced due to the charge compensation from the 3+ dopants, following ref. 58. A detailed discussion of this chemical expansion is covered in some recent literature.<sup>59–61</sup>

For the calculated bulk modulus, that of SDC (169 GPa) is found to be slightly underestimated when compared to experiments (approximately 188 GPa when considering linear Vegard's relations, *i.e.* 166 GPa for  $\text{Ce}_{0.9}\text{Sm}_{0.1}\text{O}_{1.95}$  and 195 GPa for  $\text{Ce}_{0.8}\text{Sm}_{0.2}\text{O}_{1.9}$  at room temperature).<sup>8,62</sup> For that of GDC, our calculated value of 170 GPa is also slightly underestimated when compared to experiments (about 190–200 GPa for  $\text{Ce}_{0.9}\text{Gd}_{0.1}\text{O}_{1.95}$ <sup>62,63</sup> and approximately 182–187 GPa for  $\text{Ce}_{0.9}\text{Gd}_{0.2}\text{O}_{1.9}$ <sup>63,64</sup>). However, we are in good agreement when compared to previous DFT results (*i.e.* 165 GPa for  $\text{Ce}_{0.75}\text{Gd}_{0.25}\text{O}_2$  using PBE+ $U$ ).<sup>8</sup>

Taking into account the influence of temperature on the crystal lattice, MD simulations of the SDC and GDC models are performed for various finite temperatures. In Table 1, minute lattice expansions after the MD runs are detected due to thermal vibrations and bond weakening between atoms. Considering the underestimation of bond strength by semi-local  $xc$  functionals, our DFT results do tend to show a larger value for the lattice parameters than experiments. On the other hand, our MD results nicely reproduce the lattice parameters in experiments (by construction).

Next, the RDF ( $g(r)$  in Fig. 2) as well as the bonding length profile (in Fig. 3) are examined and analyzed. The RDF has been used successfully to correlate macroscopic thermodynamics properties and the intermolecular interactions of atoms. For instance, Loya *et al.* studied  $\text{CeO}_2$  with MD and RDF to understand the self-assembly of nanoparticles.<sup>67</sup> Scavini *et al.*, reported a RDF study of GDC to clarify the complex positional disorder derived from Gd doping and oxygen vacancies formation.<sup>68</sup> These previous results strongly corroborate with our calculated RDF peaks in Fig. 2, where the first nearest neighbor (1NN) and second nearest neighbor (2NN) distance of the M–M and M–O bonds can be determined *via* the localized peaks in the calculated  $g(r)$ , from extended X-ray absorption fine

**Table 1** Calculated lattice constants of  $\text{CeO}_2$ , SDC, and GDC ( $a_{\text{CeO}_2}$ ,  $a_{\text{SDC}}$ , and  $a_{\text{GDC}}$ , respectively) given as function of temperature range

Method	$T$ (K)	$a_{\text{CeO}_2}$ (Å)	$a_{\text{SDC}}$ (Å)	$a_{\text{GDC}}$ (Å)
DFT <sup>a</sup>	0	5.49	5.51	5.50
MD <sup>a</sup>	1	5.41	5.42	5.42
MD <sup>a</sup>	300	5.42	5.43	5.43
MD <sup>a</sup>	600	5.43	5.44	5.44
MD <sup>a</sup>	1000	5.43	5.45	5.45
Experiment	300	5.42 <sup>b</sup>	5.42 <sup>c</sup>	5.42 <sup>c</sup>
DFT	0	5.49 <sup>d</sup>	5.43 <sup>e</sup>	5.43 <sup>e</sup>

<sup>a</sup> This work, PBE+ $U$ . <sup>b</sup> Ref. 65. <sup>c</sup> Ref. 66. <sup>d</sup> Ref. 48, PBE+ $U$ . <sup>e</sup> Ref. 3,  $\text{Ce}_{0.94}\text{M}_{0.06}\text{O}_{1.97}$ , PBESol+ $U$ .

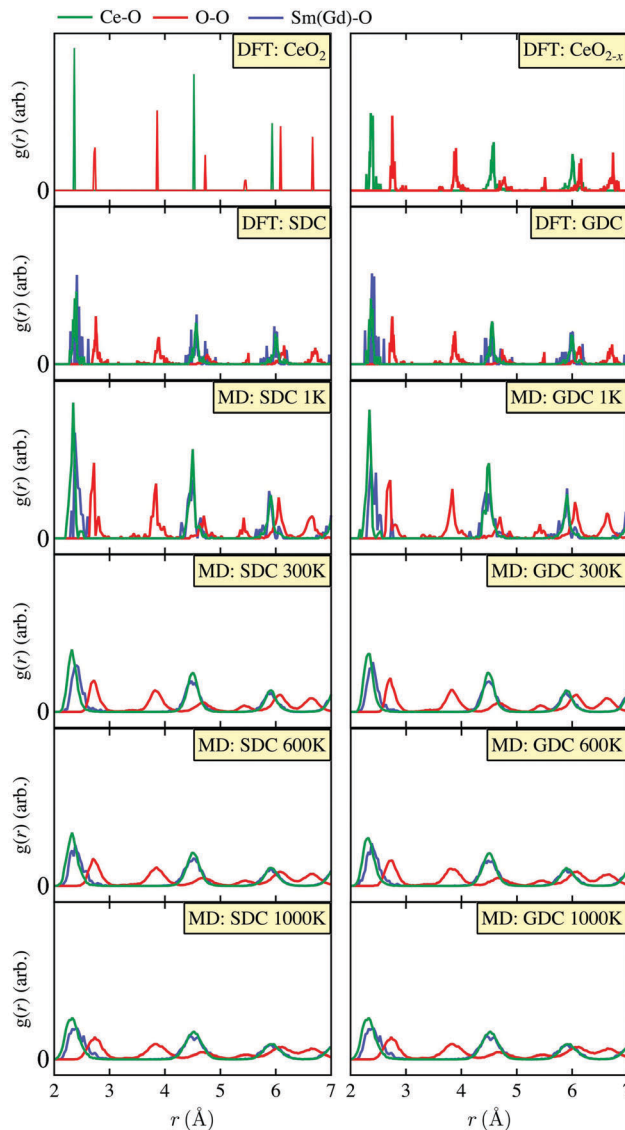


**Fig. 2** Calculated radial distribution functions (RDF) of  $\text{CeO}_2$ ,  $\text{CeO}_{2-x}$ , GDC, and SDC (as optimized with DFT at  $T = 0$  K and MD simulations at various finite temperatures). Here, the green, red, and blue lines represent the RDF between Ce–O, O–O, and dopants Sm or Gd–O.

structure (EXAFS), and the reported RDF.<sup>68</sup> Here, we note that the use of yet another structural analysis method – X-ray diffraction (XRD) of these ceria systems – agrees well with our calculated RDFs and available experiments<sup>68</sup> (as shown in Fig. 4, ESI†).

Referring to Fig. 2, the Ce–O bond lengths for pristine  $\text{CeO}_2$  can be found at 3 peak values of 2.36 Å, 4.50 Å, 6 Å. The O–O bond lengths exhibit the highest peak at 3.86 Å followed by that at 6.09 Å and 6.67 Å. Furthermore, for  $\text{CeO}_{2-x}$ , the Ce–O bond length peak at 2.36 Å has a lower intensity and exhibits broadening of peaks. While the O–O bond in  $\text{CeO}_2$  exhibits the highest peak at 3.86 Å, that in  $\text{CeO}_{2-x}$  shows the highest peak near 2.75 Å, reflecting the effect a change in cation vacancy has on the O–O bond lengths (*i.e.* broadening of peaks). We note that some re-normalized minor peaks are observed around the more intense peaks due to the existence of oxygen vacancies.

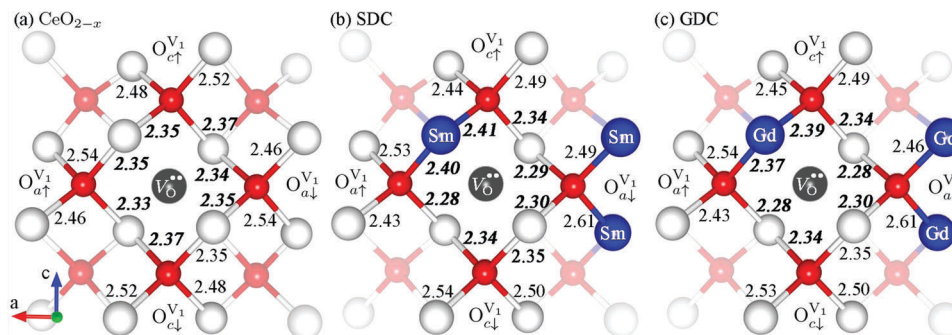


Fig. 3 Bonding length profile of DFT-optimized structures for (a)  $\text{CeO}_{2-x}$ , (b) SDC, and (c) GDC using values tabulated in Table 2. Here, the black sphere of  $V_6^*$  is taken as the vacancy ( $V_1$ ) site, and is defined as the center of the tetrahedron of nearest cations. The symbols ( $O_{a\uparrow}^{V_1}$ ,  $O_{a\downarrow}^{V_1}$ ,  $O_{c\uparrow}^{V_1}$  and  $O_{c\downarrow}^{V_1}$ ) are represented by the red spheres which are determined by the upper ( $\uparrow$ ) or lower ( $\downarrow$ ) positions in the  $a$ - and  $c$ -directions. The white and blue spheres represent the Ce and dopant (Sm or Gd) atoms. The values listed near the bonds represent the bond distances in the unit of Å.

For both SDC and GDC, the DFT-calculated  $g(r)$  of Ce–O and Sm(Gd)–O indicates the highest peak at relatively similar positions of 2.38 Å, suggesting that both the dopants occupy and replace the Ce atoms in ceria. Minor peaks are also distributed around 2.38 Å, as in  $\text{CeO}_{2-x}$ . Due to the difference in the atomic radii of  $\text{Sm}^{3+}$  and  $\text{Gd}^{3+}$ , very small shifts in Sm(Gd)–O can be observed, e.g. comparing Sm–O and Gd–O at 4.47 Å and 4.56 Å, respectively. When finite temperature (of up to 1000 K) is included, our MD-derived  $g(r)$  generally yields the same conclusions as discussed while noting that all the RDF peaks are temperature-broadened as the temperature is increased.

Given the three-dimensional spacial complexity of the distribution of oxygen ions, cations, and oxygen vacancies, we attempt to provide a bonding length profile between the cations and oxygen ions both in Fig. 3 (in the  $ac$ -plane), as well as the tabulated form in Table 2. In Table 2, we choose to discuss the bond lengths using  $d_{\pm\pm\pm}$ , where the relative position of the cation is taken with respect to the target oxygen near the vacancy along the  $a$ -,  $b$ -, and  $c$ -directions, respectively. For example,  $d_{+\uparrow}$  will represent the first nearest neighbor (1NN) cation at the upper position in the  $a$ -direction, lower position in the  $b$ -direction, and upper position in the  $c$ -direction, all taken with respect to the target oxygen ion. Here, the oxygen ions near the vacancy are also represented by a symbol, e.g.  $O_{a\uparrow}^{V_1}$ , which reflects the oxygen ion near  $V_1$  along the upper position in the  $a$ -direction. Since the profile results around  $V_1$  and  $V_2$  are almost the same, only  $V_1$  is reported.

The values with the denotation  $\vee$  represent the bonding distances between oxygens and cations nearest the oxygen vacancy site, and are found to be generally shorter than that for other cations. On the other hand, the values denoted by  $*$ , which represents the bonding distance between the oxygens and dopants, are determined to be generally longer than that for other cations. We can notice that the shortest bond length between the atoms is determined to be around 2.28–2.54 Å which corresponds well to the first highest peak in our calculated RDF results. Upon a closer look at  $\text{CeO}_{2-x}$  in Fig. 3(a), the oxygen–cation bonds near the oxygen vacancy are similar or shorter than that in  $\text{CeO}_2$  (2.38 Å), while those far from the

Table 2 Distance profile between the oxygens and cations (Ce, Sm or Gd) in the unit of Å. The  $*$  denotes dopant (Gd or Sm) and  $\vee$  denotes that the cation is close to the oxygen vacancy site. The  $d_{\pm\pm\pm}$  means the relative position of the cation with respect to the target oxygen ion near the oxygen vacancy along the  $a$ -,  $b$ -, and  $c$ -directions, respectively. For example,  $d_{+\uparrow}$  will represent the first nearest neighbor (1NN) cation at the upper position in the  $a$ -direction, lower position in the  $b$ -direction, and upper position in the  $c$ -direction, all taken with respect to the target oxygen ion. Here, the oxygen ions near the vacancy are also represented by a symbol, e.g.  $O_{a\uparrow}^{V_1}$ , which reflects the oxygen ion near  $V_1$  along the upper position in the  $a$ -direction. Since the profile results around  $V_1$  and  $V_2$  are almost the same, only  $V_1$  is reported

		$O_{a\uparrow}^{V_1}$	$O_{a\downarrow}^{V_1}$	$O_{b\uparrow}^{V_1}$	$O_{b\downarrow}^{V_1}$	$O_{c\uparrow}^{V_1}$	$O_{c\downarrow}^{V_1}$
$\text{CeO}_{2-x}$	$d_{+\uparrow}$	2.54	2.33 $\vee$	2.36 $\vee$	2.46	2.48	2.36 $\vee$
	$d_{+\downarrow}$	2.35 $\vee$	2.46	2.50	2.34 $\vee$	2.52	2.35 $\vee$
	$d_{+\uparrow}$	2.46	2.35 $\vee$	2.50	2.34 $\vee$	2.35 $\vee$	2.52
	$d_{-\downarrow}$	2.33 $\vee$	2.54	2.36 $\vee$	2.46	2.36 $\vee$	2.48
SDC	$d_{+\uparrow}$	2.53	2.28 $\vee$	2.40 $\vee^*$	2.48	2.43	2.34 $\vee$
	$d_{+\downarrow}$	2.39 $\vee^*$	2.49 $*$	2.45	2.34 $\vee$	2.48	2.35 $\vee$
	$d_{+\uparrow}$	2.43	2.30 $\vee$	2.51 $*$	2.32 $\vee$	2.41 $\vee^*$	2.54
	$d_{-\downarrow}$	2.28 $\vee$	2.61 $*$	2.31 $\vee$	2.48	2.34 $\vee$	2.50
GDC	$d_{+\uparrow}$	2.54	2.28 $\vee$	2.38 $\vee^*$	2.47	2.45	2.34 $\vee$
	$d_{+\downarrow}$	2.37 $\vee^*$	2.46 $*$	2.45	2.34 $\vee$	2.49	2.35 $\vee$
	$d_{+\uparrow}$	2.43	2.30 $\vee$	2.51 $*$	2.32 $\vee$	2.39 $\vee^*$	2.53
	$d_{-\downarrow}$	2.28 $\vee$	2.60 $*$	2.31 $\vee$	2.48	2.34 $\vee$	2.50

oxygen vacancy are much elongated to 2.46–2.52 Å – lending support to the chemical expansion of Ce atoms discussed above. For SDC and GDC, the oxygen–dopant bonds are longer (i.e. with a less strongly bound oxygen ion) near the oxygen vacancy while the opposite is true for such bonds far from the vacancy.

We further examine the structure–bonding properties in these ceria-based systems by analyzing the calculated ELF<sup>69</sup> (in Fig. 4 and Fig. S5, ESI<sup>†</sup>). The ELF plots are drawn through three specific planes with the oxygen vacancy centred/included as depicted in Fig. 4(a). Since all the defected/doped ceria systems show very similar trends in the ELF plots (in Fig. S5, ESI<sup>†</sup>), we will focus our discussion using only the SDC case, as shown in Fig. 4.

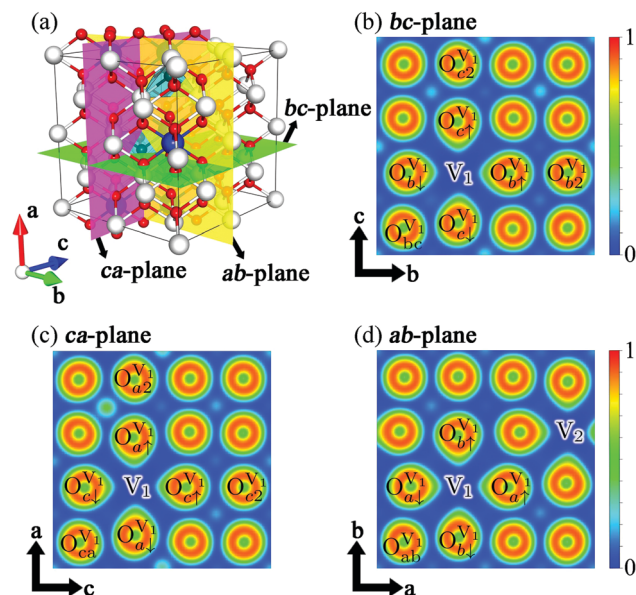


Fig. 4 Electronic localization function (ELF) plot for the oxygen vacancy (especially overlapping the one vacancy site (labelled as  $V_1$ )) along three different planes for SDC. Here, the oxygens are positioned and labelled. For example, the oxygen ion at a lower position to  $V_1$  along the  $a$ -direction is labelled as  $O_{a1}^{V1}$ .

In Fig. 4(b)–(d), we find the ELF plot for the oxygen ions near the oxygen vacancy (namely,  $O_{a1}^{V1}$ ,  $O_{a1}^{V1}$ ,  $O_{b1}^{V1}$ ,  $O_{b1}^{V1}$ ,  $O_{c1}^{V1}$  and  $O_{c1}^{V1}$ ) tends to form a noticeable distortion towards the oxygen vacancy. These ELF patterns correspond to the smaller bond distances between the oxygens in first nearest neighbor sites to the oxygen vacancy and the cations near the oxygen vacancy (marked as  $\surd$  in Table 2). On the other hand, the other oxygen

ions (namely,  $O_{a2}^{V1}$ ,  $O_{bc}^{V1}$ ,  $O_{ca}^{V1}$ ,  $O_{ba}^{V1}$ ,  $O_{b2}^{V1}$  and  $O_{c2}^{V1}$ ) maintain a symmetric spherical ELF distribution.

Through such first-principle-based structure-bonding analysis, we establish that the anisotropic distortion of oxygen atoms towards the oxygen vacancy site is evident. Although such direction-dependent distortions may be small and minute, their influence on important ion transport properties (such as lattice ionic diffusion) in ceria-based systems has not been studied. Furthermore, nor how these anisotropic lattice properties may promote/suppress lattice thermal vibrations in a specific direction of ion transport.

To investigate the influence of anisotropic distortions in oxygen atoms on their lattice thermal properties, we calculate the lattice dynamics for each ceria-based system, and further proceed to examine the related diffusion dynamics by determining the attempt frequency of oxygen ion migration.<sup>17</sup>

## B. Lattice dynamics: vibrational density-of-states

The phonon vDOS for  $\text{CeO}_2$ ,  $\text{CeO}_{2-x}$ , SDC, and GDC are calculated (see Fig. S7, ESI<sup>†</sup>) with neutron scattering weighting corrections (*cf.* eqn (1), in Fig. 5). Upon applying the neutron scattering weighting corrections, the vDOS of pristine  $\text{CeO}_2$  (Fig. 5(a)) is dominated by the oxygen modes and exhibits the highest phonon peak near the frequency mode of 56 meV, a near-zero node at 60 meV, and the second highest phonon peak located near 68 meV. Our calculated vDOS agrees well with previous reports.<sup>70</sup> The vDOS of  $\text{CeO}_{2-x}$  (Fig. 5(b)) resembles that of pristine  $\text{CeO}_2$  at lower frequencies while showing some distinct changes upon the creation of an oxygen vacancy for the higher frequency modes (more than 55 meV): softening of the second highest phonon peak (to  $\sim 62$  meV) and the disappearance of the near-zero node. For the vDOS of SDC

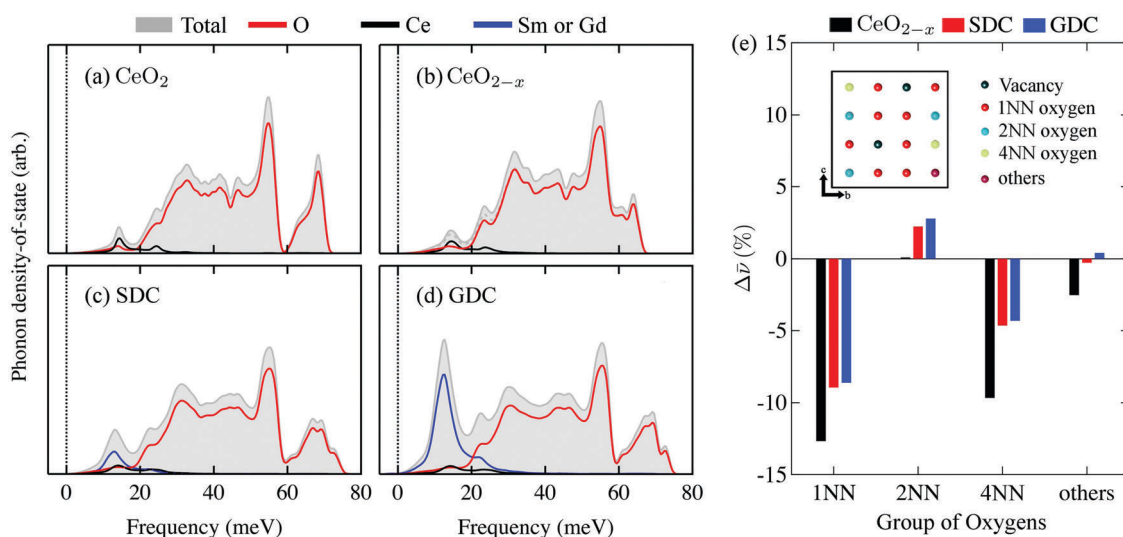


Fig. 5 The vibrational density-of-states (vDOS) (with the neutron scattering weighting corrections *cf.* eqn (1)) for (a)  $\text{CeO}_2$ , (b)  $\text{CeO}_{2-x}$ , (c) SDC, and (d) GDC, respectively. Here the gray region is the total vDOS, while the red, black, and blue lines are the vDOS of each component O, Ce and dopants (Sm or Gd), respectively. (e) The averaged changes in the center of vDOS ( $\Delta\bar{\nu}$ ) for the various oxygen ions in each ceria-based system, taken with respect to pristine  $\text{CeO}_2$ . Here,  $\Delta\bar{\nu}$  for  $\text{CeO}_{2-x}$ , SDC, and GDC are represented by the black, red, and blue bars, respectively. Benchmarked *via* the oxygen vacancy position (labelled by the black sphere in the inset), each ceria system consists of 12 1NN oxygens (red spheres), 20 2NN oxygens (cyan spheres), 4 4NN oxygens (lime spheres), and 26 other oxygens (purple spheres), respectively.

(Fig. 5(c)) and GDC (Fig. 5(d)), the second phonon peak is now shifted to 65 meV and the near-zero node at 60 meV is somewhat recovered. SDC and GDC exhibit almost the same oxygen-derived vDOS features except for the Sm- and Gd-derived phonon peaks near 10 meV (*i.e.* given that the  $\sigma_{\text{scat}}$  for Gd is about five times that of Sm).

To further understand the individual species (*i.e.* both anions and cations) contributions to the total vDOS, we calculate the representative center of the vDOS for all atoms using eqn (2) and obtain a statistical average for each species. The averaged vDOS center ( $\bar{\nu}$ ) for each species is then tabulated in Table 3, with the corresponding standard deviation value (in brackets). Comparing the values of each different system shown in Table 3, the standard deviation in the  $\bar{\nu}$  values for Ce, Sm, and Gd varies marginally across all ceria-based systems. A more distinct change is observed for the oxygen ions.

Turning our focus to the oxygen ions, we analyze the changes to their  $\bar{\nu}$  values by grouping the oxygens according to their relative positions near the oxygen vacancy. As depicted in the inset of Fig. 5(e), a schematic cartoon is shown for the first nearest neighbor (1NN), second nearest neighbor (2NN), fourth nearest neighbor (4NN) and other oxygen ions around the oxygen vacancy. Given this classification, for the ceria-based systems with two oxygen vacancies (with or without dopants, *i.e.* CeO<sub>2-x</sub>, SDC, and GDC), there will be twelve 1NN oxygens (vertical to the vacancy), twenty 2NN oxygens (diagonal to the vacancy), four 4NN oxygens, and twenty six other oxygens (purple spheres), accordingly. Considering the other oxygen vacancy within periodic boundary conditions, 6 of the 1NN oxygens will be either taken as four 2NN or two 4NN oxygens with respect to the other oxygen vacancy. The detailed tabulation of all  $\bar{\nu}$  can be found in Table S3 in the ESI.† We note that the standard deviation for each classification group is less than 1.5 meV.

Using this information, we proceed to calculate the changes to the  $\bar{\nu}$  values for each classification group of oxygens to that of oxygen in pristine CeO<sub>2</sub>. This change,  $\Delta\bar{\nu}$  is then plotted in Fig. 5(e). Interestingly, a defect/dopant-mediated softening of the 1NN and 4NN oxygen vibrational modes is observed (*i.e.* reflected by the large negative  $\Delta\bar{\nu}$  values), while the 2NN and others show a small positive  $\Delta\bar{\nu}$  value. Going back to our motivation for this classification, it then becomes clear that although the 2NN oxygens have a much shorter distance from the oxygen vacancy, the vertical positions from the vacancy

(*i.e.* the 1NN and 4NN oxygens) are most affected compared to the diagonal positions (*i.e.* the 2NN oxygens).

To better understand the influence of the oxygen vacancy on the vDOS of the different oxygens based on orientation in the lattice, we present the vDOS for all oxygens, decomposed into the three lattice directions (namely, the *a*-, *b*-, and *c*-directions) in Fig. 6. The labels in Fig. 6 follow that in Fig. 4. Here, four oxygen atoms in Fig. 6(a), (b), (d), and (e) are related to another vacancy (labelled as V<sub>2</sub>), where the detailed relations are shown in the brackets. Here, we note that the vDOS of the oxygen atoms near the oxygen vacancy in GDC and CeO<sub>2-x</sub> systems are also investigated (as shown in Fig. S8 and S9, ESI†). Comparing the vDOS of CeO<sub>2-x</sub> (Fig. S9, ESI†) to that of SDC and GDC (Fig. 5 and Fig. S8, ESI†), doping Gd or Sm to CeO<sub>2-x</sub> results in a small shifting of the oxygen vDOS peaks to higher frequencies (as illustrated in Fig. 5(b)–(d)). However, the anisotropic contributions (for each direction with respect to nearest vacancy) to the vDOS are almost identical. Due to this, we mainly use the SDC model for further discussion.

According to our nearest neighbor classification scheme, the vDOS of the 1NN oxygens are shown in Fig. 6(a), (b), (e), (f), (i) and (j). As compared to the oxygen-derived vDOS in pristine CeO<sub>2</sub>, they all exhibit a similar trend of a strong weight towards the low frequencies while broadening the phonon modes at higher frequencies. Unlike the 1NN oxygens, the vDOS of the 2NN oxygens (shown in Fig. 6(c), (g), and (k)) resemble that of the oxygen in pristine CeO<sub>2</sub>, corroborating with the very small positive  $\Delta\bar{\nu}$  (Fig. 5(e)). For the vDOS of 4NN oxygens (as seen in Fig. 6(d), (h) and (l)), an interesting observation is found: near 45 meV, especially so for that in Fig. 6(h) and (l), a very high intense localized phonon peak emerges, and this mode is not found for the other oxygens.

We rationalize that the position of the oxygen vacancy indeed influences the oxygen-derived vDOS anisotropically, *i.e.* strongly direction-dependent. For instance, in the vDOS of O<sub>a1</sub><sup>V1</sup> (Fig. 6(a)), the characteristic peak around 30 meV may be strongly attributed to the vDOS contribution along the *a*-direction (which is the direction towards V<sub>1</sub>). So generally, we find that the vDOS of the 1NN and 4NN oxygens (that is aligned vertically/orthogonally to the oxygen vacancy) tend to have a higher weight towards the low frequencies (*i.e.* generally softening), increasing the probability to vibrate in that direction towards the oxygen vacancy. To afford a more quantitative comparison, we compute the direction-dependent  $\bar{\nu}$  and list their values in Table S4 of the ESI.† In particular, we find for the 1NN and 4NN oxygens, a 20 to 30% softening of the oxygen-derived vDOS when compared to that of pristine CeO<sub>2</sub> while minimal changes are found for the 2NN oxygens. Given these clear anisotropic contributions to the overall vibrational properties of doped ceria (namely, SDC and GDC), we predict that the 1NN and 4NN oxygens may account for the higher diffusion dynamics seen in doped ceria-based SOFCs than the 2NN oxygens.

### C. Diffusion dynamics: determining the diffusion coefficient

Now, turning to the diffusion dynamics in doped ceria, finite temperature classical MD simulations have been performed for

**Table 3** The averaged center of vDOS ( $\bar{\nu}(i)$  in meV, when  $\nu(i)$  is the center of vDOS of the *i*th species *i.e.* Ce, O, and M (Sm or Gd); *cf.* eqn (2)) for pristine CeO<sub>2</sub>, CeO<sub>2-x</sub>, SDC, and GDC. Here, the values in brackets below are the standard deviation measured for each species

	CeO <sub>2</sub>	CeO <sub>2-x</sub>	SDC	GDC
$\bar{\nu}(\text{Ce})$	19.61 (0)	19.19 (0.48)	19.43 (0.66)	19.58 (0.67)
$\bar{\nu}(\text{M})$	—	—	15.85 (1.20)	15.06 (1.39)
$\bar{\nu}(\text{O})$	45.40 (0)	43.54 (2.51)	44.76 (2.17)	45.00 (2.25)

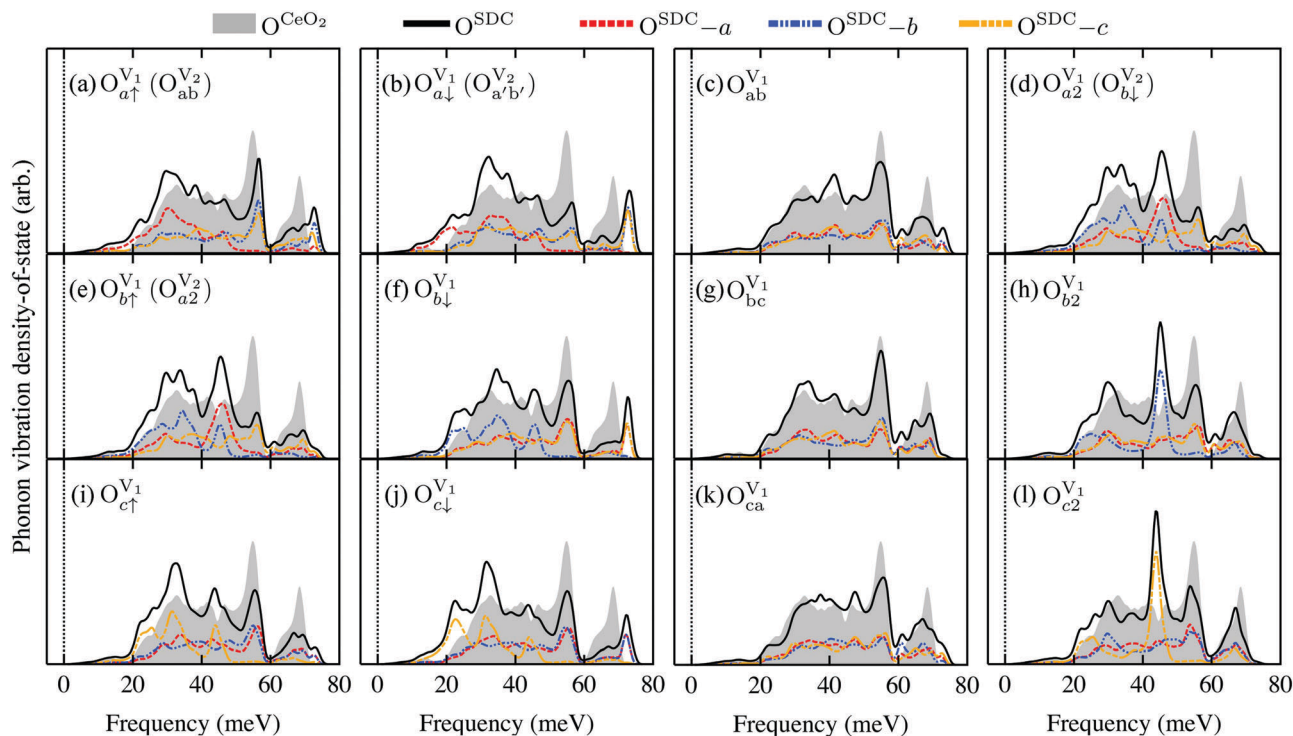


Fig. 6 Direction-dependent partial vDOS for each oxygen atom around the vacancy ( $V_1$ ) in SDC are represented with comparison to the pure  $\text{CeO}_2$  (grey region). The total and direction dependent contribution of each oxygen atom along the  $a$  direction, contribution along the  $b$  direction, and contribution along the  $c$  direction are presented as the black solid line, and the other three different colored dotted lines (red, blue and orange), respectively. With respect to the target vacancy ( $V_1$ ), the oxygens at 1NN sites are shown in the left two columns (a), (b), (e), (f), (i) and (j), the oxygens in 2NN sites are shown in the third column (c), (g), (k), and the oxygens in 4NN sites are (d), (h) and (l). Detail labels for each case follow that in Fig. 4. At (a), (b), (d), and (e), oxygens are standing in 2NN or 4NN positions with respect to another vacancy ( $V_2$ ) as labelled within the brackets. Here, we note that the GDC and  $\text{CeO}_{2-x}$  cases are presented in the ESI<sup>†</sup> due to the similarity of behavior.

the DFT-derived ordered (*i.e.* homogeneous supercell expansion of the DFT structures) and randomized SDC and GDC structures. The randomized structures of SDC and GDC are denoted as SDC(R) and GDC(R), respectively.

First of all, the  $\langle R^2 \rangle$  of oxygen ions has been calculated. It increases linearly with time, and the slope is almost constant for all SDC and GDC models at each temperature, shown in Fig. 7(a) and (d) for the ordered SDC and GDC structures, respectively. The diffusion coefficient,  $D$  for the various models of SDC and GDC are given in Table S5 in the ESI.<sup>†</sup> From these values, we have found that  $D$  of the ordered SDC and GDC are  $0.97 \times 10^{-12}$  and  $0.78 \times 10^{-12}$ , respectively, whereas  $D$  values of  $(1.07\text{--}1.59) \times 10^{-12}$  and  $(1.11\text{--}1.37) \times 10^{-12}$  are found for SDC(R) and GDC(R), respectively.

Similarly, the  $\langle R^2 \rangle$  is also computed along the orthogonal  $a$ -,  $b$ -, and  $c$ -directions. Within the accuracy of numerical noise, we find a small anisotropic behavior in the direction-dependent  $\langle R^2 \rangle$  for both SDC and GDC. In particular, the computed  $\langle R^2 \rangle$  is very similar along the  $a$ - and  $c$ -directions whereas a slightly smaller value is found in the  $b$ -direction, as indicated in Fig. 7(b) and (e). Our classical MD diffusion dynamics analysis corroborates very well with the DFT-derived vDOS analysis above, with both demonstrating similar trends of anisotropic phonon mode softening for the oxygen ions near the oxygen vacancy. Here, we note that this element-dependent  $\langle R^2 \rangle$  variation

is clearly found in both DFT-derived ordered models as well as randomized ones. Furthermore, the  $\langle R^2 \rangle$  of the cations (Ce, Sm and Gd) is not changed within the simulation time (as indicated by the horizontal lines in Fig. 7(b) and (e)). Hence, the cations are not expected to diffuse and only exhibit vibrational features around their lattice sites at finite temperatures. The oxygen ions, on the other hand, clearly show migratory behavior from one lattice site to another (or a vacancy site) at these temperatures.

It is known that the conductivity and the ion diffusion coefficient,  $D$  are proportional with temperature while the activation energy barrier,  $E_a$ , may somewhat vary for different temperature regimes.<sup>17,71</sup> At low temperatures,  $E_a$  may fluctuate and subsequently stabilize at higher temperatures. The reason for this is, at low temperatures, vacancy-dopant and vacancy-oxygen ion interactions are dominant, whereas this interaction energy barrier may be overcome for mobile oxygen ions at higher temperatures.

Using linearized Arrhenius relations, we have also computed  $E_a$  for both ordered and randomized SDC and GDC models at temperatures ranging from 700 to 1800 K. We have found that for the SDC(R) and GDC(R) models, the calculated diffusion coefficients tend to show a larger error bar at low temperatures, while these error bars are greatly reduced in the high temperature regime. Averaging all the  $D$  values for the randomized models, we plot the diffusion coefficient ( $\log D$ ) as a function of

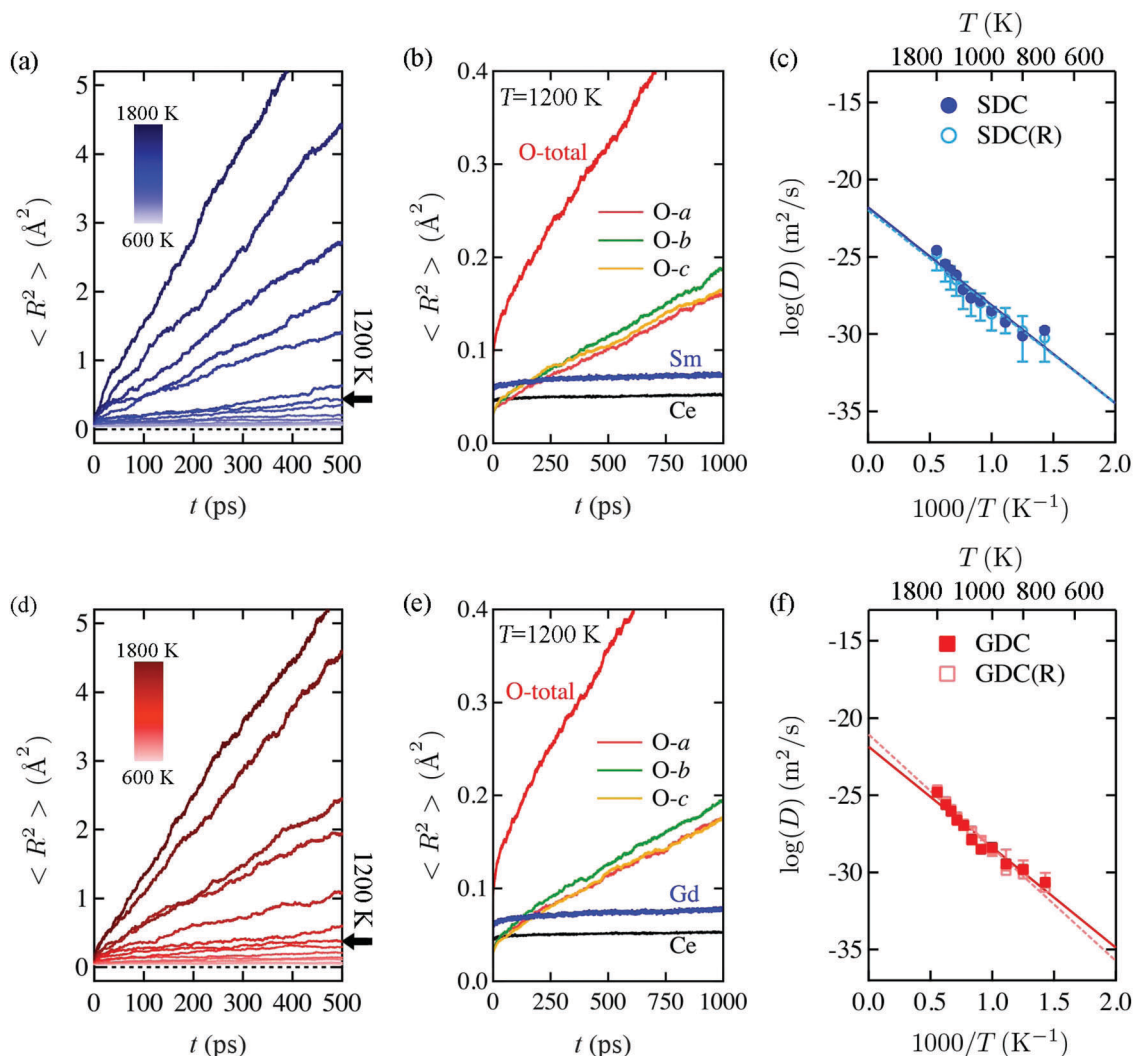


**Fig. 7** The mean square displacement,  $\langle R^2 \rangle$  of ordered (a) SDC and (d) GDC, as a function of time ( $t$ ) for various finite temperatures, ranging from 600 to 1800 K, following the blue and red monochromatic color bars in each graph, respectively. The  $\langle R^2 \rangle$  for each species in (b) SDC and (e) GDC is also plotted for  $T = 1200$  K as a function of  $t$ . Here, the black, blue and red lines denote the total  $\langle R^2 \rangle$  of Ce, dopant (Sm or Gd), and O, respectively. Additionally, the pink, green, and orange lines represent the direction-dependent  $\langle R^2 \rangle$  for the oxygen ions along the orthogonal  $a$ -direction (O- $a$ ),  $b$ -direction (O- $b$ ) and  $c$ -direction (O- $c$ ), respectively. Finally, the Arrhenius plots of the diffusion coefficient ( $\log(D)$ ) for the ordered SDC and GDC, and 5 different randomized structures each for SDC and GDC (labelled as SDC(R) and GDC(R), respectively) are plotted as a function of  $1000/T$ . Here, the absolute temperatures, the corresponding  $T$  are shown in the upper horizontal axis for each  $1000/T$ . In (c) and (f), the blue (red) straight and cyan (pink) dashed lines are obtained from a linear regression fit for each data set of ordered and randomized SDC (GDC) structures.

$1000/T$  via a linear regression fit and find very similar  $E_a$  values for the ordered cases (0.52 eV for SDC and 0.55 eV for GDC) and randomized cases (0.51 eV with  $\pm 0.039$  eV for SDC(R) and 0.59 eV with  $\pm 0.034$  eV for GDC(R)), as illustrated in Fig. 7(c) and (f). Here, we find very good agreement with experimentally determined  $E_a$  values for RE-doped ceria (e.g. 0.62 to 0.64 eV for Gd and Sm co-doped ceria<sup>10,72</sup>).

## IV. Conclusions

In this work, we have examined the structural, vibrational, and diffusion properties of different ceria-based systems including oxygen vacancies and RE dopants (Sm or Gd) – both using

first-principles DFT calculations and finite temperature MD simulations. Based on the different lattice structure analysis approaches such as bond length profiling, simulated RDF and XRD plots, phonon vDOS of the ceria-based systems, we find that the 1NN and 4NN oxygens clearly exhibit orientation-dependent phonon mode softening. Of these, we also unequivocally demonstrate that this phonon mode softening is anisotropic and direction-dependent, especially in the orthogonal/vertical directions towards the oxygen vacancy. In addition, the diffusion dynamics for both ordered and randomized SDC and GDC models were studied and we report the diffusion coefficient and energy activation barrier for these doped ceria systems. We envisage that the anisotropic influence of oxygen vacancies on the oxygen ion mobility (especially for the 1NN and 4NN sites) will

provide a platform for further analysis of ion transport mechanisms in doped fluorite-structured electrolytes.

## Conflicts of interest

There are no conflicts to declare.

## Acknowledgements

We gratefully acknowledge support by Samsung Research Funding Center of Samsung Electronics under Project Number SRFC-MA1501-03. Computational resources have been provided by the KISTI supercomputing center (KSC-2017-C3-0059) and the Australian National Computational Infrastructure (NCI). We thank Seungwon Chio and Jiwon Park for discussion.

## References

- 1 J.-h. Myung, H. J. Ko, J.-J. Lee, J.-H. Lee and S.-H. Hyun, Synthesis and Characterization of NiO/GDC-GDC Dual Nano-Composite Powders for High-Performance Methane Fueled Solid Oxide Fuel Cells, *Int. J. Hydrogen Energy*, 2012, **37**, 11351–11359.
- 2 H. J. Ko, J.-h. Myung, J.-H. Lee, S.-H. Hyun and J. S. Chung, Synthesis and Evaluation of  $(\text{La}_{0.6}\text{Sr}_{0.4})(\text{Co}_{0.2}\text{Fe}_{0.8})\text{O}_3(\text{LSCF})-\text{Y}_{0.08}\text{Zr}_{0.92}1.96(\text{YSZ})-\text{Gd}_{0.1}\text{Ce}_{0.9}\text{O}_{2-\delta}$  (GDC) Dual Composite SOFC Cathodes for High Performance and Durability, *Int. J. Hydrogen Energy*, 2012, **37**, 17209–17216.
- 3 M. Alaydrus, M. Sakaue and H. Kasai, A DFT+*U* Study On the Contribution of 4f Electrons to Oxygen Vacancy Formation and Migration in Ln-Doped  $\text{CeO}_2$ , *Phys. Chem. Chem. Phys.*, 2016, **18**, 12938–12946.
- 4 K. Kim, J. D. Yoo, S. Lee, M. Bae, J. Bae, W. Jung and J.-W. Han, A Simple Descriptor to Rapidly Screen Co Oxidation Activity On Rare-Earth Metal-Doped  $\text{CeO}_2$ : From Experiment to First-Principles, *ACS Appl. Mater. Interfaces*, 2017, **9**, 15449–15458.
- 5 D. A. Andersson, S. I. Simak, N. V. Skorodumova, I. A. Abrikosov and B. Johansson, Optimization of Ionic Conductivity in Doped Ceria, *Proc. Natl. Acad. Sci. U. S. A.*, 2006, **103**, 3518–3521.
- 6 S. Kuharungrong, Ionic Conductivity of Sm, Gd, Dy and Er-Doped Ceria, *J. Power Sources*, 2007, **171**, 506–510.
- 7 P. P. Dholabhai and J. B. Adams, A Blend of First-Principles and Kinetic Lattice Monte Carlo Computation to Optimize Samarium-Doped Ceria, *J. Mater. Sci.*, 2012, **47**, 7530–7541.
- 8 D. E. P. Vanpoucke, P. Bultinck, S. Cottenier, V. Van Speybroeck and I. Van Driessche, Aliovalent Doping of  $\text{CeO}_2$ : DFT Study of Oxidation State and Vacancy Effects, *J. Mater. Chem. A*, 2014, **2**, 13723–13737.
- 9 S. Omar, E. D. Wachsman, J. L. Jones and J. C. Nino, Crystal Structure-Ionic Conductivity Relationships in Doped Ceria Systems, *J. Am. Ceram. Soc.*, 2009, **92**, 2674–2681.
- 10 B. Steele, Appraisal of  $\text{Ce}_{1-y}\text{Gd}_y\text{O}_{2-y/2}$  Electrolytes for IT-SOFC Operation at 500 C, *Solid State Ionics*, 2000, **129**, 95–110.
- 11 W. Zajac and J. Molenda, Electrical Conductivity of Doubly Doped Ceria, *Solid State Ionics*, 2008, **179**, 154–158.
- 12 P. P. Dholabhai, J. B. Adams, P. Crozier and R. Sharma, A Density Functional Study of Defect Migration in Gadolinium Doped Ceria, *Phys. Chem. Chem. Phys.*, 2010, **12**, 7904–7907.
- 13 A. Ismail, J. Hooper, J. B. Giorgi and T. K. Woo, A DFT+*U* Study of Defect Association and Oxygen Migration in Samarium-Doped Ceria, *Phys. Chem. Chem. Phys.*, 2011, **13**, 6116–6119.
- 14 C. W. Huang, W. C. J. Wei, C. S. Chen and J. C. Chen, Molecular Dynamics Simulation on Ionic Conduction Process of Oxygen in  $\text{Ce}_{1-x}\text{M}_x\text{O}_{2-x/2}$ , *J. Eur. Ceram. Soc.*, 2011, **31**, 3159–3169.
- 15 J. O. Nilsson, M. Leetmaa, O. Y. Vekilova, S. I. Simak and N. V. Skorodumova, Oxygen diffusion in ceria doped with rare-earth elements, *Phys. Chem. Chem. Phys.*, 2017, **19**, 13723–13730.
- 16 G. H. Vineyard, Frequency Factors and Isotope Effects in Solid State Rate Processes, *J. Phys. Chem. Solids*, 1957, **3**, 121–127.
- 17 J. Koettgen, T. Zacherle, S. Grieshammer and M. Martin, *Ab Initio* Calculation of the Attempt Frequency of Oxygen Diffusion in Pure and Samarium Doped Ceria, *Phys. Chem. Chem. Phys.*, 2017, **19**, 9957–9973.
- 18 S. Grieshammer, T. Zacherle and M. Martin, Entropies of Defect Formation in Ceria From First Principles, *Phys. Chem. Chem. Phys.*, 2013, **15**, 15935–15938.
- 19 Y. Xie, H.-Y. Cao, Y. Zhou, S. Chen, H. Xiang and X.-G. Gong, Oxygen Vacancy Induced Flat Phonon Mode at  $\text{FeSe}/\text{SrTiO}_3$  Interface, *Sci. Rep.*, 2015, **5**, 10011.
- 20 G. Kresse and J. Furthmüller, Efficiency of *Ab Initio* Total Energy Calculations for Metals and Semiconductors Using a Plane-Wave Basis Set, *Comput. Mater. Sci.*, 1996, **6**, 15–50.
- 21 G. Kresse and J. Furthmüller, Efficient Iterative Schemes for *Ab Initio* Total-Energy Calculations Using a Plane-Wave Basis Set, *Phys. Rev. B: Condens. Matter Mater. Phys.*, 1996, **54**, 11169–11186.
- 22 P. E. Blöchl, Projector Augmented-Wave Method, *Phys. Rev. B: Condens. Matter Mater. Phys.*, 1994, **50**, 17953–17979.
- 23 G. Kresse and D. Joubert, From Ultrasoft Pseudopotentials to the Projector Augmented-Wave Method, *Phys. Rev. B: Condens. Matter Mater. Phys.*, 1999, **59**, 1758.
- 24 J. P. Perdew, K. Burke and M. Ernzerhof, Generalized Gradient Approximation Made Simple, *Phys. Rev. Lett.*, 1996, **77**, 3865.
- 25 J. L. F. Da Silva, M. V. Ganduglia-Pirovano and J. Sauer, Formation of the Cerium Orthovanadate  $\text{CeVO}_4$ : DFT+*U* Study, *Phys. Rev. B: Condens. Matter Mater. Phys.*, 2007, **76**, 125117.
- 26 M. Fronzi, A. Soon, B. Delley, E. Traversa and C. Stampfl, Stability and Morphology of Cerium Oxide Surfaces in an Oxidizing Environment: A First-Principles Investigation, *J. Chem. Phys.*, 2009, **131**, 104701.

- 27 J. P. Poirier and A. Tarantola, A Logarithmic Equation of State, *Phys. Earth Planet. Inter.*, 1998, **109**, 1.
- 28 A. Otero-de-la-Roza and V. Luaña, GIBBS2: A New Version of the Quasi-Harmonic Model Code. I. Robust Treatment of the Static Data, *Comput. Phys. Commun.*, 2011, **182**, 1708–1720.
- 29 S. Le Roux and P. Jund, Ring Statistics Analysis of Topological Networks: New Approach and Application to Amorphous GeS<sub>2</sub> and SiO<sub>2</sub> Systems, *Comput. Mater. Sci.*, 2010, **49**, 70–83.
- 30 S. Le Roux and P. Jund, Erratum: Ring Statistics Analysis of Topological Networks: New Approach and Application to Amorphous GeS<sub>2</sub> and SiO<sub>2</sub> Systems, *Comput. Mater. Sci.*, 2010, **49**, 70–83.
- 31 F. Izumi and K. Momma, Three-Dimensional Visualization in Powder Diffraction, *Solid State Phenom.*, 2007, **130**, 15–20.
- 32 K. Momma and F. Izumi, VESTA: A three-dimensional visualization system for electronic and structural analysis, *J. Appl. Crystallogr.*, 2008, **41**, 653–658.
- 33 A. Togo and I. Tanaka, First Principles Phonon Calculations in Materials Science, *Scr. Mater.*, 2015, **108**, 1–5.
- 34 Y. Wang, S.-L. Shang, H. Fang, Z.-K. Liu and L.-Q. Chen, First-principles calculations of lattice dynamics and thermal properties of polar solids, *npj Comput. Mater.*, 2016, **2**, 16006.
- 35 Z.-W. Niu, Z.-Y. Zeng, C.-E. Hu, L.-C. Cai and X.-R. Chen, Study of the thermodynamic properties of CeO<sub>2</sub> from *ab initio* calculations: The effect of phonon-phonon interaction, *J. Chem. Phys.*, 2015, **142**, 014503.
- 36 V. F. Sears, Neutron Scattering Lengths and Cross Sections, *Neutron News*, 1992, **3**, 26–37.
- 37 D. Phelan, J. N. Millican, E. L. Thomas, J. B. Leão, Y. Qiu and R. Paul, Neutron Scattering Measurements of the Phonon Density of States of FeSe<sub>1-x</sub> Superconductors, *Phys. Rev. B: Condens. Matter Mater. Phys.*, 2009, **79**, 014519.
- 38 C. W. Li, H. L. Smith, T. Lan, J. L. Niedziela, J. A. Muñoz, J. B. Keith, L. Mauger, D. L. Abernathy and B. Fultz, Phonon Anharmonicity of Monoclinic Zirconia and Yttrium-Stabilized Zirconia, *Phys. Rev. B: Condens. Matter Mater. Phys.*, 2015, **91**, 144302.
- 39 B. Silvi and A. Savin, Classification of chemical bonds based on topological analysis of electron localization functions, *Nature*, 1994, **371**, 683–686.
- 40 *Large-scale Atomic/Molecular Massively Parallel Simulator (LAMMPS)*, <http://lammps.sandia.gov>.
- 41 S. Plimpton, Fast Parallel Algorithms for Short-Range Molecular Dynamics, *J. Comput. Phys.*, 1995, **117**, 1–19.
- 42 L. Minervini, R. W. Grimes and K. E. Sickafus, Disorder in pyrochlore oxides, *J. Am. Ceram. Soc.*, 2000, **83**, 1873–1878.
- 43 M. Pirzada, Oxygen Migration in A<sub>2</sub>B<sub>2</sub>O<sub>7</sub> Pyrochlores, *Solid State Ionics*, 2001, **140**, 201–208.
- 44 A. Gotte, D. Spangberg, K. Hermansson and M. Baudin, Molecular Dynamics Study of Oxygen Self-Diffusion in Reduced CeO<sub>2</sub>, *Solid State Ionics*, 2007, **178**, 1421–1427.
- 45 M. Rushton, A. Chroneos, S. Skinner, J. Kilner and R. Grimes, Effect of Strain On the Oxygen Diffusion in Ytria and Gadolinia Co-Doped Ceria, *Solid State Ionics*, 2013, **230**, 37–42.
- 46 M. A. Kovalenko and A. Y. Kupryazhkin, Melting and Superionic Transition of Gd-Doped Ceria Nanocrystals: Molecular Dynamics Study, *J. Nucl. Mater.*, 2012, **430**, 12–19.
- 47 A. Einstein, On The Motion Of Small Particles Suspended In Liquids At Rest Required By The Molecular-kinetic Theory Of Heat, *Ann. Phys.*, 1905, **17**, 549–560.
- 48 J. L. F. Da Silva, M. V. Ganduglia-Pirovano, J. Sauer, V. Bayer and G. Kresse, Hybrid Functionals Applied to Rare-Earth Oxides: the Example of Ceria, *Phys. Rev. B: Condens. Matter Mater. Phys.*, 2007, **75**, 045121.
- 49 L. Gerward and J. S. Olsen, Powder Diffraction Analysis of Cerium Dioxide at High Pressure, *Powder Diffr.*, 1993, 127–129.
- 50 M. G. Chourashiya, J. Y. Patil, S. H. Pawar and L. D. Jadhav, Studies On Structural, Morphological and Electrical Properties of Ce<sub>1-x</sub>Gd<sub>x</sub>O<sub>2-(x/2)</sub>, *Mater. Chem. Phys.*, 2008, **109**, 39–44.
- 51 X. Guan, H. Zhou, Z. Liu, Y. Wang and J. Zhang, High Performance Gd<sup>3+</sup> and Y<sup>3+</sup> Co-Doped Ceria-Based Electrolytes for Intermediate Temperature Solid Oxide Fuel Cells, *Mater. Res. Bull.*, 2008, **43**, 1046–1054.
- 52 B. Li, X. Wei and W. Pan, Improved Electrical Conductivity of Ce<sub>0.9</sub>Gd<sub>0.1</sub>O<sub>1.95</sub> and Ce<sub>0.9</sub>Sm<sub>0.1</sub>O<sub>1.95</sub> by Co-Doping, *Int. J. Hydrogen Energy*, 2010, **35**, 3018–3022.
- 53 S. Omar, E. D. Wachsman and J. C. Nino, Higher Ionic Conductive Ceria-Based Electrolytes for Solid Oxide Fuel Cells, *Appl. Phys. Lett.*, 2007, **91**, 144106.
- 54 V. V. Ivanov, V. R. Khrustov, Y. A. Kotov, A. I. Medvedev, A. M. Murzakaev, S. N. Shkerin and A. V. Nikonov, Conductivity and Structure Features of Ce<sub>1-x</sub>Gd<sub>x</sub>O<sub>2-δ</sub> Solid Electrolytes Fabricated by Compaction and Sintering of Weakly Agglomerated Nanopowders, *J. Eur. Ceram. Soc.*, 2007, **27**, 1041–1046.
- 55 Y.-P. Fu, Y.-S. Chang and S.-B. Wen, Microwave-Induced Combustion Synthesis and Electrical Conductivity of Ce<sub>1-x</sub>Gd<sub>x</sub>O<sub>2-1/2x</sub> Ceramics, *Mater. Res. Bull.*, 2006, **41**, 2260–2267.
- 56 Z. Tianshu, Ionic Conductivity in the CeO<sub>2</sub>Gd<sub>2</sub>O<sub>3</sub> System (0.05 ≤ Gd/Ce ≤ 0.4) Prepared by Oxalate Coprecipitation, *Solid State Ionics*, 2002, **148**, 567–573.
- 57 J. Hooper, A. Ismail, J. B. Giorgi and T. K. Woo, Computational Insights Into the Nature of Increased Ionic Conductivity in Concentrated Samarium-Doped Ceria: A Genetic Algorithm Study, *Phys. Chem. Chem. Phys.*, 2010, **12**, 12969–12972.
- 58 D. Marrocchelli, S. R. Bishop, H. L. Tuller and B. Yildiz, Understanding Chemical Expansion in Non-Stoichiometric Oxides: Ceria and Zirconia Case Studies, *Adv. Funct. Mater.*, 2012, **22**, 1958–1965.
- 59 S. R. Bishop, Chemical expansion of solid oxide fuel cell materials: A brief overview, *Acta Mech. Sin.*, 2013, **29**, 312–317.
- 60 D. Marrocchelli, C. Chatzichristodoulou and S. R. Bishop, Defining chemical expansion: the choice of units for the stoichiometric expansion coefficient, *Phys. Chem. Chem. Phys.*, 2014, **16**, 9229–9232.

- 61 M. Heidenreich, C. Kaps, A. Simon, F. Schulze-Küppers and S. Baumann, Expansion behaviour of (Gd,Pr)-substituted CeO<sub>2</sub> in dependence on temperature and oxygen partial pressure, *Solid State Ionics*, 2015, **283**, 56–67.
- 62 T. Kushi, K. Sato, A. Unemoto, S. Hashimoto, K. Amezawa and T. Kawada, Elastic Modulus and Internal Friction of SOFC Electrolytes at High Temperatures Under Controlled Atmospheres, *J. Power Sources*, 2011, **196**, 7989–7993.
- 63 A. Atkinson and A. Selçuk, Mechanical Behaviour of Ceramic Oxygen Ion-Conducting Membranes, *Solid State Ionics*, 2000, **134**, 59–66.
- 64 T. Kushi, K. Sato, A. Unemoto, K. Amezawa and T. Kawada, Investigation of High Temperature Elastic Modulus and Internal Friction of SOFC Electrolytes Using Resonance Method, *ECS Trans.*, 2009, **25**, 1673–1677.
- 65 L. Gerward, J. Staun Olsen, L. Petit, G. Vaitheeswaran, V. Kanchana and A. Svane, Bulk Modulus of CeO<sub>2</sub> and PrO<sub>2</sub> – An Experimental and Theoretical Study, *J. Alloys Compd.*, 2005, **400**, 56–61.
- 66 S. Zha, C. Xia and G. Meng, Effect of Gd (Sm) Doping On Properties of Ceria Electrolyte for Solid Oxide Fuel Cells, *J. Alloys Compd.*, 2003, **115**, 44–48.
- 67 A. Loya, J. L. Stair and G. Ren, Simulation and Experimental Study of Rheological Properties of CeO<sub>2</sub>-Water Nanofluid, *Int. Nano Lett.*, 2015, **5**, 1–7.
- 68 M. Scavini, M. Coduri, M. Allieta, M. Brunelli and C. Ferrero, Probing Complex Disorder in Ce<sub>1-x</sub>Gd<sub>x</sub>O<sub>2-x/2</sub> Using the Pair Distribution Function Analysis, *Chem. Mater.*, 2012, **24**, 1338–1345.
- 69 V. Tsirelson and A. Stash, Determination of the Electron Localization Function From Electron Density, *Chem. Phys. Lett.*, 2002, **351**, 142–148.
- 70 Y. Wang, L. A. Zhang, S. Shang, Z.-K. Liu and L.-Q. Chen, Accurate Calculations of Phonon Dispersion in CaF<sub>2</sub> and CeO<sub>2</sub>, *Phys. Rev. B: Condens. Matter Mater. Phys.*, 2013, **88**, 024304.
- 71 M. Kamiya, E. Shimada, Y. Ikuma, M. Komatsu and H. Haneda, Intrinsic and Extrinsic Oxygen Diffusion and Surface Exchange Reaction in Cerium Oxide, *J. Electrochem. Soc.*, 2000, **147**, 1222–1227.
- 72 B. Li, X. Wei and W. Pan, Improved Electrical Conductivity Of Ce<sub>0.9</sub>Gd<sub>0.1</sub>O<sub>1.95</sub> and Ce<sub>0.9</sub>Sm<sub>0.1</sub>O<sub>1.95</sub> By Co-doping, *Int. J. Hydrogen Energy*, 2010, **35**, 3018–3022.